Convective systems and rainfall in East Africa

Article

Published Version

Hill, P. G. ORCID: https://orcid.org/0000-0002-9745-2120, Stein, T. H. M. ORCID: https://orcid.org/0000-0002-9215-5397 and Cafaro, C. ORCID: https://orcid.org/0000-0001-8063-4887 (2023) Convective systems and rainfall in East Africa. Quarterly Journal of the Royal Meteorological Society, 149 (756). pp. 2943-2961. ISSN 1477-870X doi: 10.1002/qj.4540 Available at https://centaur.reading.ac.uk/112685/

To link to this article DOI: http://dx.doi.org/10.1002/qj.4540

Publisher: Royal Meteorological Society

Received: 30 September 2022 | Revised: 24 May 2023 | Accepted: 22 June 2023

DOI: 10.1002/qj.4540

Quarterly Journal of the Royal Meteorological Society RMetS

RESEARCH ARTICLE

Convective systems and rainfall in East Africa

Peter G. Hill[1] | **Thorwald H. M. Stein**[1] | **Carlo Cafaro**[2]

[1]Department of Meteorology, University of Reading, Reading, UK

[2]MetOffice@Reading, University of Reading, Reading, UK

Correspondence
Peter G. Hill, University of Reading,
Meteorology Building, Earley Gate,
Reading, RG6 6BB, UK.
Email: p.g.hill@reading.ac.uk

Funding information
Global Challenges Research Fund,
Grant/Award Number: NE/P021077/1

Abstract

East Africa is particularly vulnerable to weather extremes, with severe weather linked to thousands of deaths per year. Improved forecasts of convective events in this region are urgently needed, from both nowcasting and numerical weather prediction models. Improving these forecasts requires further knowledge of convection in this region. This study aims to improve understanding of convective events in East Africa, based on a six-year climatology of convective life cycles and the associated precipitation. Convective systems are identified as contiguous areas of cold cloud in geostationary satellite measurements over East Africa. A tracking algorithm is used to trace the evolution of the properties of these systems through time and space. Matching the systems to surface precipitation obtained from satellite microwave observations provides insight into how the life cycles of these systems relate to precipitation at the surface. Over the region as a whole, 59% of the accumulated precipitation can be attributed to the tracked convective systems. The majority (81%) of heavy precipitation events ($\geq 10\,\mathrm{mm\cdot hr^{-1}}$) are attributable to convective systems, while light rainfall events ($<1\,\mathrm{mm\cdot hr^{-1}}$) are not (1.8%). Most of the tracked convective systems have an area less than $400\,\mathrm{km^2}$ and last for less than an hour. However, the less frequent larger longer-lived systems produce the majority of the regional accumulated precipitation. Composite life cycles of the tracked systems show rapid intensification and the heaviest precipitation initially, followed by a steady increase in area and weakening in intensity before the system decays. Finally, the Madden–Julian oscillation, which plays a key role in intraseasonal rainfall variability in the region, is also linked to the amount of rainfall due to convective systems through changes in the frequency and properties of these systems.

KEYWORDS

atmosphere, clouds, convection, mesoscale, observational data analysis, rainfall, Tropics

1 | INTRODUCTION

East Africa is a region that is remarkably vulnerable to weather and climate variability. East Africa is notably arid compared with other tropical landmasses (e.g. Yang *et al.*, 2015) and frequent droughts have severe impacts for water resources, agriculture, and the health of the local population (e.g. Haile *et al.*, 2019). However, extreme

---

weather and flooding also cause major problems. Severe weather over Lake Victoria causes thousands of deaths by drowning each year (e.g. Kobusingye *et al.*, 2016; Whitworth *et al.*, 2019), and the broader region suffers some of the highest occurrences of both flood disasters and deaths due to flood disasters in Africa (Li *et al.*, 2016; Watkiss and Cimato, 2021; Roberts *et al.*, 2022). Climate change is likely to exacerbate these problems, with the frequency of heavy rainfall events in East Africa expected to increase (Bornemann *et al.*, 2019).

In this context there is a clear need for accurate and reliable weather forecasting systems and climate predictions for East Africa, yet both still suffer from significant inadequacies in this region. Climate models fail to reproduce extremely wet days in East Africa (Ayugi *et al.*, 2021), and even though high-resolution convection-permitting climate models show improved representations of the diurnal cycle and intensity of East African rainfall, large biases in the seasonal mean remain (Finney *et al.*, 2019). Similarly, numerical weather prediction models generally have large rainfall errors in East Africa (e.g. Wang *et al.*, 2022). Indeed even computationally expensive convection-permitting ensembles have less skill over East Africa than is typical for midlatitudes (Cafaro *et al.*, 2021). This suggests that addressing the problems modelling convective events in this region requires an improved understanding of local convective systems and their drivers.

Recent research has identified satellite-derived nowcasting products as a promising alternative source of short-range forecasts for East Africa (e.g. Roberts *et al.*, 2021). However, these nowcasts also have large biases and errors (e.g. Hill *et al.*, 2020). These errors may be linked to the fact that many of these nowcasting products were developed for midlatitudes. Consequently, as for models, improving nowcasts requires improved understanding of local convective systems. In addition, improving nowcasts will require better knowledge of the links between the properties of convection that can be observed by geostationary satellites and the surface precipitation produced. Despite the vulnerability of East Africa to severe weather, satellite studies of convective systems in this region are much rarer than in West Africa (e.g. Taylor *et al.*, 2011; Klein *et al.*, 2018; Baidu *et al.*, 2022), where mesoscale convective systems are more common (Laing and Fritsch, 1993; Hodges and Thorncroft, 1997). Consequently, knowledge of the behaviour of convective systems in East Africa remains relatively poor.

Although convective-scale phenomena are poorly understood and predicted in East Africa, the precipitation climatology of the region is relatively well documented (e.g. Nicholson, 2017; Camberlin, 2018). East Africa is a meteorologically complex region, with large temporal and spatial variability. Much of this spatial variability is tied to the surface topography, with complex orography, the presence of large inland lakes, and the Indian Ocean coastline all influencing mesoscale circulations and hence local precipitation. Lake Victoria in particular stands out, receiving increased rainfall due to its unique topography (e.g. Woodhams *et al.*, 2019) and showing less seasonal variability than the rest of the region. At the regional scale, the large seasonal rainfall variability has been linked to changes in the western Indian Ocean sea-surface temperature (Yang *et al.*, 2015), with warmer temperatures in the short and long wet seasons (October–November–December (OND) and March–April–May (MAM), respectively) and colder temperatures in the dry seasons (January–February (JF) and June–July–August–September (JJAS)). However, a deeper understanding of the seasonal cycle still needs to be developed (Nicholson, 2018).

There is also a growing understanding of the drivers of precipitation variability at intraseasonal and interannual scales (e.g. Nicholson, 2017). Of particular note, the Madden–Julian Oscillation (MJO: Madden and Julian (1971)) plays a dominant role in East African intraseasonal precipitation variability (Pohl *et al.*, 2005). The relationship between the MJO and rainfall varies across the region, with suppressed rainfall near the coast and enhanced rainfall in the highlands for early-phase MJO and vice versa for later-phase MJO (e.g. Omeny *et al.*, 2006; Pohl and Camberlin, 2006; Hogan *et al.*, 2014). Recent research has linked the MJO to extreme rainfall events associated with flooding in the East African highlands region (MacLeod *et al.*, 2021). However, how the MJO links to convective scales in East Africa remains an open question.

Motivated by the need to improve understanding of convective systems, this article aims to address three research questions.

1. How much of the precipitation in East Africa is due to deep convective systems, and how does this vary with season, location, and time of day?
2. How do the properties of these convective systems evolve over the life cycle of the system, and how do these properties link to the precipitation produced by the convective system?
3. How do these relationships between convective systems and precipitation relate to the Madden–Julian Oscillation?

In order to tackle these questions, a climatology of tracked convective systems over East Africa has been generated. The climatology covers the period from 2014 to 2019 inclusive and is based on identification and tracking of convective systems using geostationary infrared satellite data. Corresponding precipitation estimates have been obtained from the aggregated microwave measurements from various polar low-orbit satellites in the *Global Precipitation Measurement Mission*(*GPM*) Integrated Multi-satellitE Retrievals for *GPM* (IMERG) product. This unique new dataset of convective systems proves to be an excellent tool for understanding the relationships between precipitation and convective-system properties in East Africa.

This article is organised as follows. The following section describes the observational data used in this study and the algorithm that is used to track convective systems through time. Section 3 quantifies the contribution of the tracked convective systems to precipitation in East Africa. Section 4 examines how the properties of the convective systems relate to the precipitation they produce, while Section 5 focuses on the life cycles of these properties. Section 6 identifies MJO impacts on the properties of the tracked convective systems. Finally, Section 7 brings the article to a close with a brief discussion of the results.

2 | METHODS

2.1 | Brightness temperature data and identification of convective systems

The identification and tracking of convective systems is based on 10.8-μm brightness temperatures (BTs) from the Spinning Enhanced Visible and InfraRed Imagers (SEVIRI) on board the *MeteoSat Second Generation* geostationary satellites located above 0°N, 0°E. The tracking covers the period from January 1, 2014–January 1, 2020, in order to match the availability of the *GPM* radar data for another study. SEVIRI measures BTs for the disc centred at 0°N, 0°E every 15 min with a resolution of approximately 3 km at nadir. The "simple-track" software used to track the systems requires the input data to be on a regular grid, so these BTs are first regridded using bilinear interpolation onto an equal area projection with 4.4-km resolution extending from 23°W–57°E and 15°S–25°N.

Convective systems are identified using these 10.8-μm BTs and a threshold of 233 K, which is a widely used threshold for identifying cold cloud (e.g. Laurent *et al.*, 1998; Laing *et al.*, 2008; Goyens *et al.*, 2011; Taylor *et al.*, 2011). Contiguous areas of BT less than this threshold are identified using eight-point connectivity, with a minimum convective system size of 18 pixels, which corresponds to an area of ~350 km^2. Although this minimum size is somewhat arbitrary, analysis in Section 4 demonstrates that these smallest systems are very short-lived and, although they are numerous, contribute very little to the total regional accumulated precipitation.

2.2 | Tracking software

Once convective systems have been identified, they can be traced through time. This is based on the "simple-track" algorithm,[1] which has previously been used to track convective systems in models and radar observations over the UK (Stein *et al.*, 2014) and South Africa (Keat *et al.*, 2019) and precipitation datasets over Africa (Crook *et al.*, 2019).

The first step is to use an optical flow technique to derive displacement vectors that are used to advect the systems forward to the next image. These vectors are the displacements that maximise the correlation between successive brightness temperature fields. The vectors are calculated separately for subregions of 48 × 48 grid boxes, each separated by 24 grid boxes. These separate vectors are then interpolated linearly to the full domain to get a full velocity field. Using only the convective systems (i.e., BTs less than 233 K) to derive the displacement vectors discards potentially useful information from warmer pixels. However, using the full BT field means lower altitude warm clouds that may be moving at different speeds, and static surface features such as coastlines will affect the calculation of the displacement vector. As a compromise between these two extremes, we use only BTs less than 273.15 K to calculate the displacement vectors, by setting BTs warmer than this threshold to 273.15 K.

Once the velocity field is calculated, each of the convective systems at time t is advected to a new location using the mean of the velocity field for that system. The advected systems from time t are then compared with systems at time $t+1$ and an overlap fraction is calculated for each possible pair of convective systems. This overlap fraction f is calculated using Equation 1, where $|A|$ is the number of pixels in convective system A and $|A \cap B|$ is the number of pixels in both A and B:

$$f = \frac{|A \cap B|}{|A|} + \frac{|A \cap B|}{|B|}. \tag{1}$$

Following the approach used in the Thunderstorm Identification, Tracking, Analysis, and Nowcasting (TITAN) storm-tracking algorithm (Dixon and Wiener, 1993; Han *et al.*, 2009) and subsequently in all previous studies using this "simple-track" algorithm (Stein *et al.*, 2014; Crook *et al.*, 2019; Keat *et al.*, 2019), if this overlap fraction is larger than 0.6, then the system at time $t+1$ inherits the history of the system from time t. If multiple systems from time t have an overlap fraction of 0.6 with the same system at time $t+1$, then the history is inherited from the system with the largest overlap fraction and the other systems are labelled as "accreted". Similarly, if multiple systems at

---

[1] https://github.com/thmstein/simple-track

time $t + 1$ have an overlap fraction greater than 0.6 with the same system from time t, then the system at time $t + 1$ with the largest overlap fraction inherits the history and the other systems at time $t + 1$ are labelled as "children" of the "parent" system from time t. Using this tracking algorithm, the properties of each convective system can be followed through time. These properties include the identifier, area, location, and advection of the system, a record of interactions with other systems, and various attributes of the brightness temperature within the system.

This tracking is run for the entire period from January 1, 2014–January 1, 2020 using the 15-min SEVIRI temporal resolution. From this large dataset of convective systems, all those systems that have any point coinciding with the East Africa domain are then extracted for this study. For the purposes of this study, East Africa denotes the region bounded by 30°E, 10°S, 52°E, and 12°N. If SEVIRI measurements for one or more pixels in the broader tropical Africa domain are missing, the tracking is simply restarted from the next point in time that has a complete set of brightness-temperature observations. Systems with a start or end time that cannot be determined conclusively due to missing observations are excluded from the final dataset. Over the six-year period, the algorithm tracks 989,928 convective systems over East Africa. Of these 989,928 convective systems 6,173 have either a start or end time that cannot be determined conclusively due to missing observations. These 6,173 are excluded from the final dataset, resulting in 983,755 convective systems. This large number of systems facilitates a detailed statistical analysis of convective systems in the following sections.

2.3 | Rainfall data

Rainfall observations from the *GPM* (Hou *et al.* (2014)) IMERG (Huffman *et al.* (2019)) version 6 final dataset are used in order to understand the links between the tracked convective systems and precipitation. The IMERG dataset provides rainfall estimates with a temporal resolution of 30 min on a fixed latitude–longitude grid with a resolution of 0.1°. However, to ensure that the rainfall estimate is independent of the geostationary observations used to identify convective systems, we only use the "high-quality" rainfall estimates, which are those estimates that are derived directly from passive microwave radiometer observations. These correspond to around 30% of pixels over East Africa in the IMERG version 6 dataset. This is necessary because the spatially complete rainfall estimates rely on the same geostationary observations that are used to identify convective systems in this study. Focusing on high-quality data also results in a more accurate rainfall estimate (e.g. Tan *et al.*, 2016).

For comparison with the convective systems, the IMERG data is regridded onto the higher resolution 4.4-km grid used for the convective systems using the nearest-neighbour method. With the IMERG rainfall data and the convective systems on the same grid, the IMERG rainfall estimate for each pixel in each convective system can be extracted. However, as the microwave measurements used for the high-quality IMERG dataset are not always available, there is no rainfall estimate for many pixels. For each point in the life cycle of each convective system, if there is a valid IMERG high-quality rainfall estimate for each pixel in the system at that point in time, then the mean and maximum rain rate and rain fraction are calculated and stored. If any IMERG high-quality rainfall estimates are missing for the system at that point in the life cycle, then these are instead set as missing data indicators.

For the analysis of the contribution of convective systems to the total rainfall in the region, the method described in the previous paragraph to assign rainfall to convective systems may lead to an underestimate of the convective contribution. This is because, when a convective system is partially overlapped with an IMERG pixel, either in space or time, the method implicitly assumes the rainfall is equally spread between the convective and nonconvective parts of the IMERG pixel, whereas in reality it may be expected to be concentrated in the convective area. To quantify the uncertainty due to partial overlap between IMERG pixels and convective systems, two other rainfall estimates are also produced. In the first, all the rainfall in partially overlapped cases is assumed to be convective. In the second, all the rainfall in partially overlapped cases is assumed to be nonconvective.

2.4 | MJO

Analysis of the impact of the MJO on convective systems is based on the Wheeler and Hendon (2004) index.[2] This index is based on two empirical orthogonal functions calculated for a combination of zonal wind at two altitudes (850 and 200 hPa) and outgoing longwave radiation (OLR) at the top of the atmosphere. The zonal wind fields used to calculate the MJO index are taken from the National Centers for Environmental Prediction (NCEP) reanalysis, while the OLR is obtained from satellite measurements.

The relationship between the MJO and precipitation varies across East Africa, with contrasting effects inland and near the coast (e.g. Pohl and Camberlin, 2006; Berhane and Zaitchik, 2014; Hogan *et al.*, 2014). In order to ensure

---

[2] This was obtained from http://www.bom.gov.au/climate/mjo/graphics/rmm.74toRealtime.txt

a strong and consistent relationship between the MJO and rainfall, the analysis of the effect of the MJO on convective system properties is restricted to inland (10°S–10°N and 30°–38°E). Only active MJO days, defined here as days when the amplitude of the MJO index is greater than one, are used to identify the impact of the MJO.

3 | CONTRIBUTION OF CONVECTIVE SYSTEMS TO EAST AFRICA PRECIPITATION

This study of East African convective systems is primarily motivated by the associated surface precipitation. Geostationary satellite measurements as used to identify convective systems in this study are often also used to identify precipitation due to the excellent temporal and spatial coverage they provide and a long history demonstrating the relationships between brightness temperatures and precipitation (e.g. Arkin, 1979; Milford and Dugdale, 1990). Modern algorithms for identifying precipitation in geostationary satellite data have useful skill (e.g. Marcos *et al.*, 2015). However, they are not perfect, and, despite the development of increasingly sophisticated methods, large errors remain and even intense precipitation events are sometimes missed altogether (e.g. Hill *et al.*, 2020). With this knowledge, we do not expect all intense precipitation events in East Africa to be identified as convective systems in our dataset, which uses a simple brightness-temperature threshold applied to a single channel. As the associated surface precipitation is the prime motivation for studying convective systems in this study, it is useful to understand the fraction of East African precipitation occurrences that can be attributed to our tracked convective systems and how this depends on location and rainfall intensity.

Figure 1 shows the fraction of IMERG high-quality rainfall events that can be associated with convective systems over the entire time period and region. For the purposes of this figure (and Figures 2 and 3), each precipitating IMERG pixel at each point in time counts as a single rainfall event. The darker bars show the fractional contribution of rainfall events of different intensities to the total number of rainfall events, while the lighter bars show the fraction of these rainfall events that coincide with a tracked convective system. The majority of precipitating pixels are of low intensity ($< 0.5\,\mathrm{mm{\cdot}hr^{-1}}$) and only a small fraction of these are associated with our tracked convective systems. This is consistent with previous analysis of the fraction of precipitation events due to warm rain, which showed that fewer than half the rainfall events in East Africa involve cold clouds (Field and Heymsfield, 2015). However, more intensely precipitating pixels, which occur less frequently, are more likely to coincide with a convective system. These more heavily precipitating events provide the majority of the precipitation in the region. Consequently, convective systems provide more than half the annual rainfall in the region.

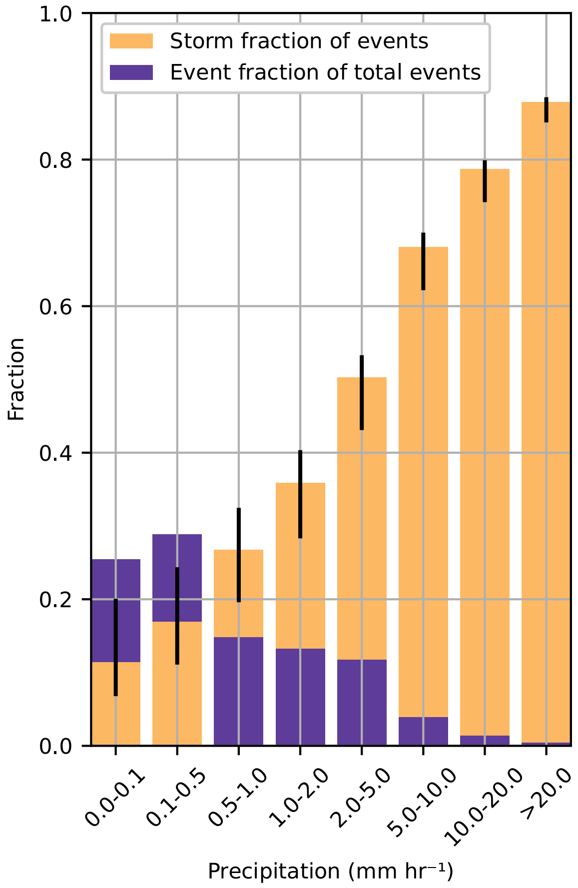

FIGURE 1 Fractional contribution of tracked convective systems to occurrence of rainfall events of differing intensities and the fraction of rainfall events with these intensities. Error bars show the range from including only rainfall events that are fully within a tracked convective system to including any rainfall events that overlap with any tracked convective system. [Colour figure can be viewed at wileyonlinelibrary.com]

As detailed in Section 2.3, the method for identifying the contribution of convective systems to the precipitation is likely to be somewhat conservative; only the fraction of each IMERG pixel that is covered by a convective system is attributed to convection. The error bars show results from alternative methods for identifying the contribution of convective systems to the precipitation. The upper limit shows the case where the entire IMERG pixel is attributed to convection if it partially overlaps with a system, while the lower limit shows the case where the IMERG rainfall is only attributed to convection if the whole IMERG pixel lies within a convective system. Parallax uncertainty

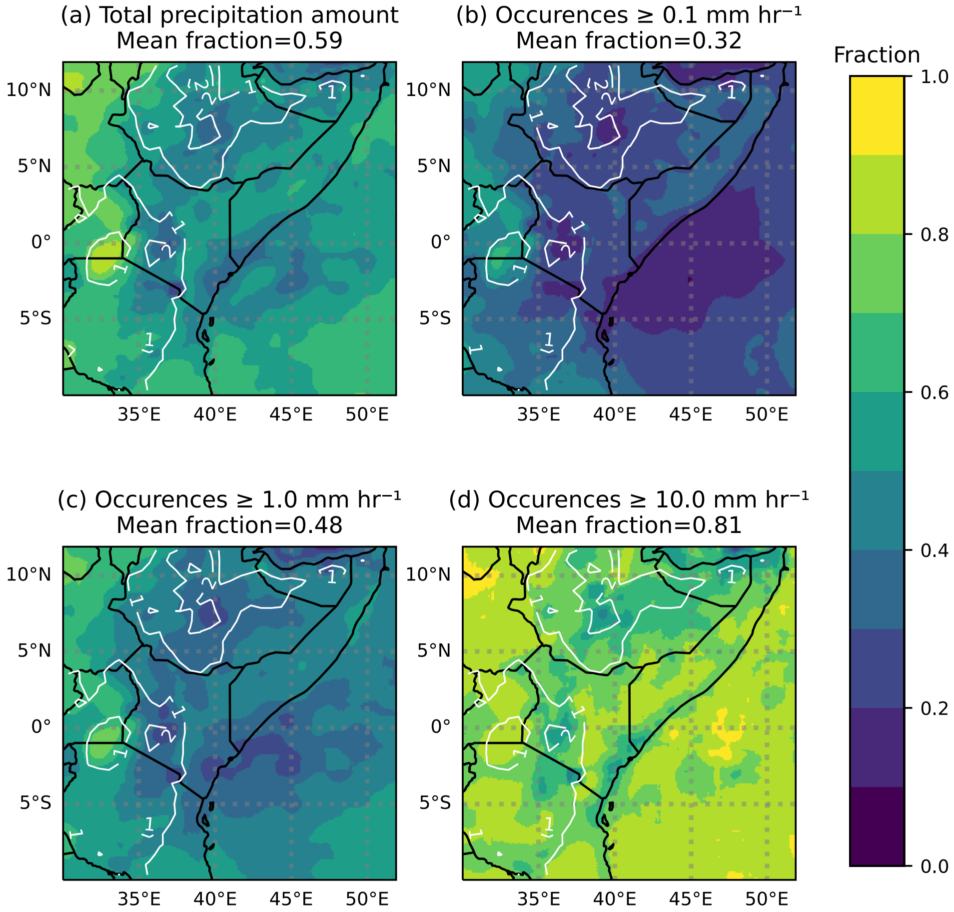
(a) Total precipitation amount Mean fraction=0.59

(b) Occurences ≥ 0.1 mm hr⁻¹ Mean fraction=0.32

(c) Occurences ≥ 1.0 mm hr⁻¹ Mean fraction=0.48

(d) Occurences ≥ 10.0 mm hr⁻¹ Mean fraction=0.81

FIGURE 2 Fractional contribution of tracked convective systems to (a) total accumulated precipitation amount and (b–d) occurrence of precipitation events above the given intensity. White contours indicate the surface altitude in kilometres. [Colour figure can be viewed at wileyonlinelibrary.com]

(e.g. Johnson *et al.*, 1994) for SEVIRI and differences in observation time between SEVIRI and the microwave instruments used in IMERG also contribute uncertainty to the co-location of precipitation and convective systems. Indeed, by adding precipitation that is within 20 km of a convective system, the percentage of accumulated precipitation due to convection increases from 59% to 79% and the percentage of intense ($\geq 10\,\text{mm}\cdot\text{hr}^{-1}$) events attributable to convection increases from 81% to 91%. The remaining 9% of intense precipitation events that are not attributable to the tracked convective systems may be due to convective cloud tops that are warmer than 233 K, or convective systems that are too small (fewer than 18 pixels in size) to be included in the tracking.

Figure 2 shows how the fraction of rainfall that can be attributed to convective systems varies throughout the region. Figure 2a shows the fraction of the total rainfall (i.e., amount) that can be attributed to convective systems, while Figure 2b–d shows the fraction of rainfall events (i.e., occurrence) of the given intensity that can be attributed to convective systems. There is significant spatial variability in both the fraction of total precipitation and the fraction of rainfall events that can be attributed to convective systems. These spatial patterns are generally consistent across all four panels. However, they do vary significantly across seasons (e.g., Supplementary Figures S3–S6), with larger fractions in regions that receive more rainfall in that season. Notable minima in the annual fraction are linked to orography (indicated by the white contours), and are seen over the Kenyan and southern Somalian coast. These minima appear consistently across all seasons and are thought to relate to warm rain linked to orographic precipitation (e.g. Young *et al.*, 2018) and sea breezes, respectively. On the other hand, over Lake Victoria, which is a noted hotspot for severe convective storms (e.g. Woodhams *et al.*, 2019; Hanley *et al.*, 2021), a large fraction of precipitation events of all intensities and total precipitation is attributed to convective systems across all four seasons.

In Figure 3 we investigate the diurnal cycle of the fraction of precipitation that can be attributed to convective systems. The diurnal cycle of total precipitation (Figure 3a) shows a minimum at 1000 and maximum at 1600 local time, which is typical of tropical land areas (e.g. Liu and Zipser, 2008). This is also consistent with the dominant peak times for rainfall over land in East Africa as identified by Camberlin *et al.* (2017). The diurnal cycles of rainfall events exceeding 0.1 and $1.0\,\text{mm}\cdot\text{hr}^{-1}$ are very similar, but intense precipitation has a weaker diurnal cycle, with a larger fraction occurring overnight. This is

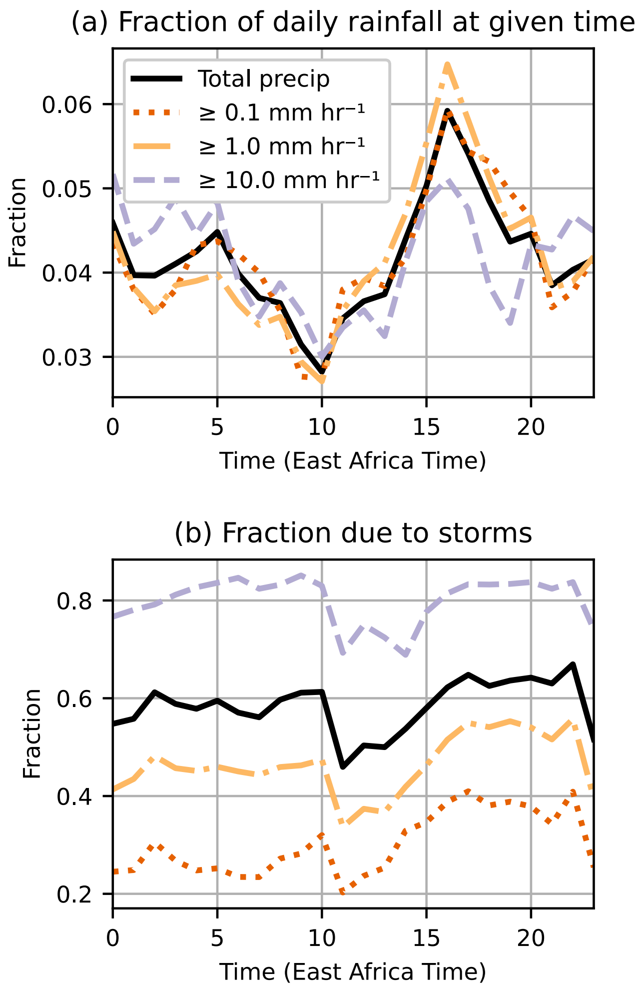

FIGURE 3 Diurnal cycle of (a) precipitation and (b) contribution of convective systems to precipitation. The solid line shows the fraction of total precipitation amount and broken lines show the fraction of occurrence of precipitation events exceeding the given threshold. [Colour figure can be viewed at wileyonlinelibrary.com]

likely due to the fact that a disproportionate fraction of the most intense events occur over Lake Victoria (e.g., Supplementary Figures S1 and S2), which has a quite different diurnal cycle due to lake and land-breeze effects (e.g. Camberlin *et al.*, 2017; Wilson and Roberts, 2022). There are subtle differences in the diurnal cycle across the four seasons, particularly for the occurrence of intense rainfall (e.g., Supplementary Figures S7–S10) that warrant further investigation beyond the scope of this study.

The diurnal cycle of the fraction of rainfall that can be attributed to convective systems is shown in Figure 3b. The diurnal cycle for total precipitation and those for different precipitation thresholds all have quite small amplitudes (approximately 0.2), with a minimum one hour after the minimum of the precipitation diurnal cycle at 1100 local time. This lag is consistent with the 233-K brightness-temperature threshold struggling to capture precipitation in the early stages of the convective life cycle. A larger fraction of precipitation can be attributed to convective systems in the afternoon than in the morning, with the difference increasing for lower intensity systems, possibly because lower intensity events are more likely to be due to warm or orographic rain, which may not have specific diurnal cycles. Since convection does have a diurnal cycle, this leads to a higher contribution from convection in the most active phase of the convection diurnal cycle.

We have demonstrated that the convective systems we have tracked play a key role in regional precipitation, contributing the majority of the accumulated rainfall amount (59%; Figure 2a) throughout most of the day and representing the vast majority of intense events (81%; Figure 2d). The subsequent analysis aims to understand how the properties of these convective systems relate to surface precipitation.

4 | PROPERTIES OF CONVECTIVE SYSTEMS AND THEIR LINKS TO SURFACE PRECIPITATION

In this section we consider the relationships between the different properties of the tracked convective systems, including how these properties relate to each other and how they link to the surface precipitation.

Figure 4 shows the distributions of the lifetime and mean area of the convective systems for each season and the codistribution of convective system areas and lifetimes including all seasons. Most convective systems are short-lived (Figure 4a), with the modal lifetime being 15 min (i.e., the system is detected in only a single image). The frequency decreases rapidly and consistently as the lifetime increases (note the log–log scale). All four seasons show a similarly shaped distribution, with more systems of all lifetimes in the long wet season (MAM). Most systems are small (Figure 4b), with the modal area being 19 pixels (recall from Section 2 that areas smaller than 18 pixels are not counted as convective systems). The frequency of convective systems decreases rapidly with increasing mean area and all four seasons show a similarly shaped distribution, with more systems of all sizes in the long wet season (MAM).

The codistribution of convective system lifetimes and areas (Figure 4c) shows that they are positively correlated, with a Pearson product–moment correlation coefficient of 0.57. The most common duration systems, which do not last long enough to be detected in more than one image, are generally also very small, with a median area of 27 pixels and a model area of only 18 pixels (i.e., the minimum possible area). Longer-lived systems tend to be

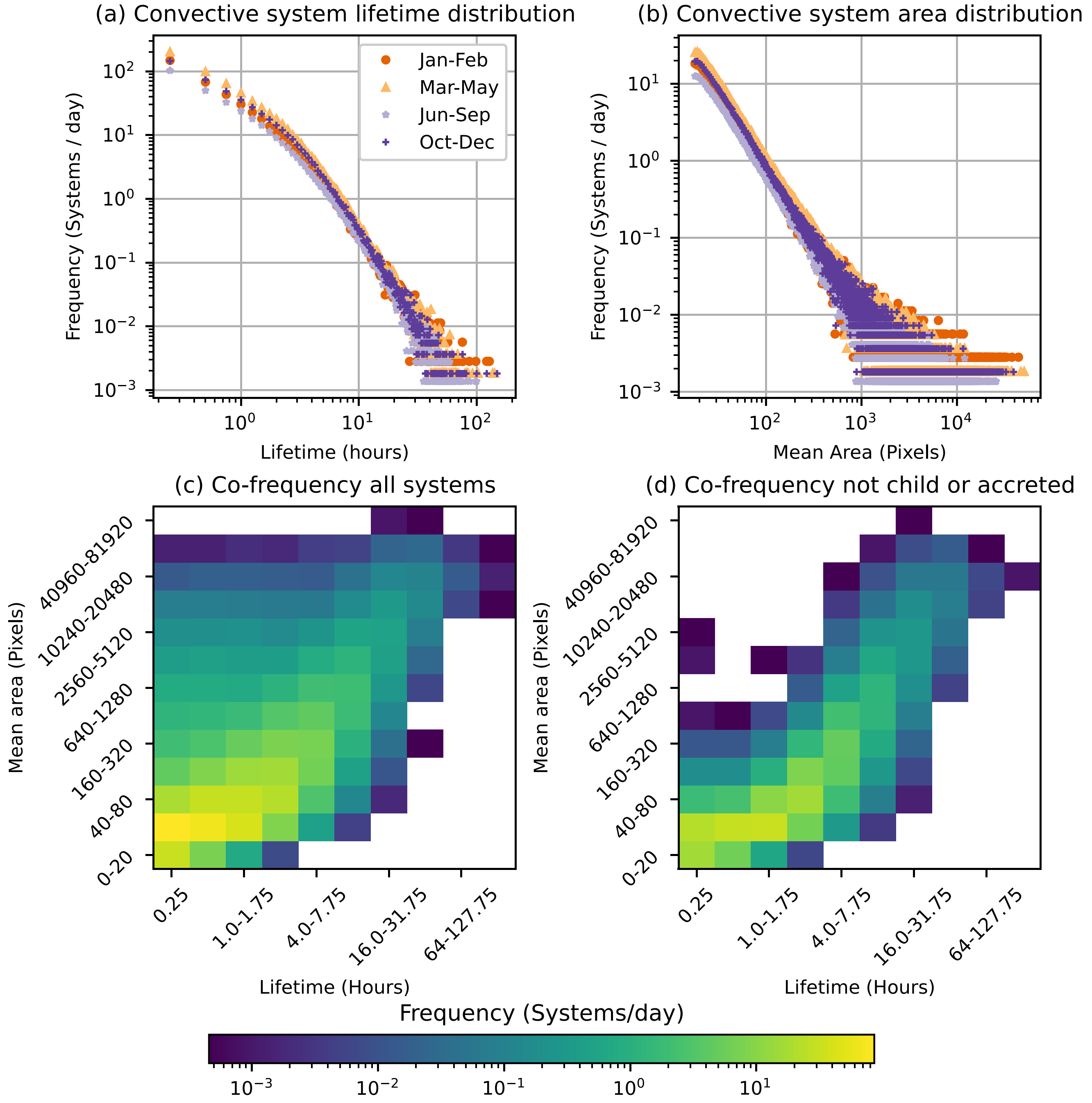

FIGURE 4 Distribution of East African convective system lifetimes and mean areas. (a,b) Distribution of convective system lifetimes and mean areas, respectively, for the four seasons and all systems. (c) Codistribution of convective system lifetimes and mean areas for all systems and all four seasons combined. (d) Codistribution for all four seasons combined, but excluding systems that are either initiated as children (i.e., due to fracturing of existing systems) or end by being accreted by another system. [Colour figure can be viewed at wileyonlinelibrary.com]

larger and larger systems tend to be longer-lived, despite the prevalence of short-lived systems. There appears to be an upper limit to the lifetime of small systems. For example, the smallest systems all last less than four hours. On the other hand, short-lived systems can be very large, with areas exceeding 20,000 pixels for systems that last for just a single image. Further analysis (Figure 4d and Supplementary Figure S11) reveals that all the systems that last only a single timestep and are larger than 5,120 pixels are children of previously existing systems (i.e., they are initiated by a previous system fracturing into multiple systems) and >90% are accreted by other systems (i.e., they end due to merging with another system). That is, they are fragments of longer-lived systems that appear briefly as separate systems. This is discussed further in Section 5. Note that if child or accreted systems are excluded, the correlation between lifetime and size increases to 0.68.

Figure 5 shows the mean and fraction of total precipitation, and the fraction of systems that produce heavy (i.e., exceeding 10 mm·hr^{-1}) rainfall, for convective systems of different lifetimes and mean areas. Note that IMERG high-quality precipitation measurements are only available for the region approximately 33% of the time, which decreases the signal-to-noise ratio, particularly for the largest and most long-lived systems, which are less frequent. The mean precipitation (averaged across all the pixels in a system and the lifetime of the system) generally increases for larger and longer-lived systems (Figure 5a). However, there is some evidence of a decrease in mean precipitation for small systems that are particularly long-lived and for the largest longer-lived (i.e., more than 4 hr) systems. The longer-lived small systems tend to initiate earlier in the day than the other systems (not shown), which suggests that this is nonconvective cirrus rather than lingering anvil cloud. On the other hand, the decrease in mean precipitation for the largest longer-lived systems is likely due to a large amount of anvil cloud, which doesn't produce precipitation.

Figure 5b, shows that despite occurring less frequently, larger longer-lived convective systems contribute a larger fraction of the total regional precipitation. One might think that large long-lived systems contribute most because they simply cover a larger area and last more time (by definition), but they also have higher mean precipitation rates, which is not a given. This large contribution to regional precipitation from large long-lived systems is consistent with previous analysis of rain-gauge data, which showed that most of the precipitation in East Africa was due to infrequent intense long-lived systems (Dezfuli *et al.*, 2017).

From a nowcasting perspective, it is important to note both the total precipitation from a system and the likelihood of receiving extreme localised rainfall. In Figure 5c, the fraction of systems of a given area and lifetime that have a maximum rain rate greater than 10 mm·hr^{-1} at any time is shown. Evidently, larger longer-lived systems are more likely to produce heavy rainfall, while this fraction is low for the numerous small systems. This is useful information for nowcasting purposes, when the number of active systems can be overwhelming.

5 | LIFE CYCLES OF CONVECTION IN EAST AFRICA

In order to ensure the results are meaningful, our analysis of convective life cycle focuses on systems that last for

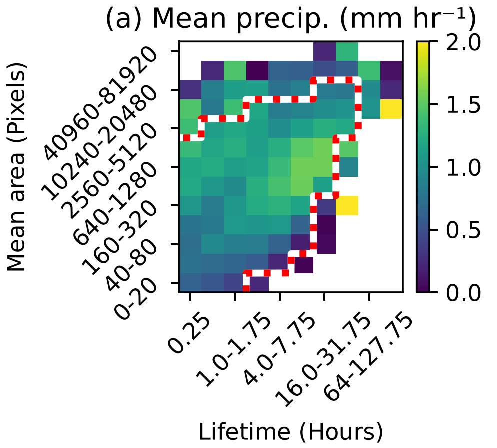

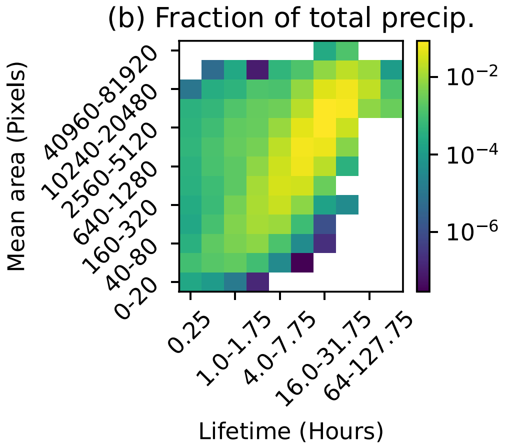

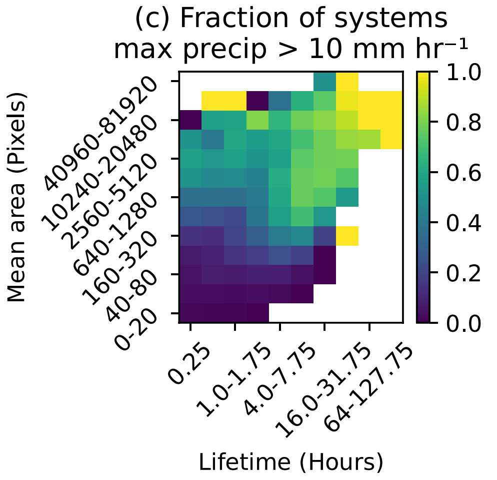

FIGURE 5 (a) Mean precipitation averaged over the lifetime and area of the convective system. The dotted contour encloses the points where there are more than 100 samples. (b) Fractional contribution from convective systems in each lifetime and mean area bin to the total accumulated precipitation amount. (c) Fraction of convective systems in each mean area and lifetime bin with maximum precipitation (over the entire area and lifetime of the system) larger than 10 mm·hr^{-1}. [Colour figure can be viewed at wileyonlinelibrary.com]

at least one hour (four SEVIRI timesteps) and have mean area larger than 40 pixels. This excludes many short-lived and/or small systems. The cycles of systems that last less than an hour are not sampled sufficiently frequently to conduct meaningful analysis, while systems that are less than 40 pixels in mean area are constrained to remain small throughout their life cycle by the fact that their mean area is small. Moreover systems that last less than an hour or have a mean area less than 40 pixels contribute very little of the regional precipitation (Figure 5b). Consequently; although they account for 51.5% of the systems, they contribute only 1.8% of the total rainfall amount. Figure 6 shows the life cycle of the area of convective systems of duration 1, 2, 4, and 8 hr (4, 8, 16, and 32 SEVIRI timesteps) and three mean area bins. The left column shows the life cycle for all systems that last for each of these times in the given mean area bin. As highlighted in the previous section, interactions between systems play a significant role in the relationship between area and lifetime. To address this, the plots in the right column, systems that are children (i.e., that form due to fracturing of an existing system) or accreted (i.e., that end due to merging with another system), are excluded.

Focusing first on those systems with initiation and end that are independent of other systems (i.e., the right column), systems generally have the smallest mean area at the start and end of their life cycles, with maximum mean area very shortly after halfway through the system lifetime. The exceptions to this are short-lived large systems, which have maximum mean area much closer to the end of their life cycle and decay much more rapidly. Restricting the life cycles further to those systems that do not have any interactions with other systems (not shown), the rapid decrease in area does not occur. This suggests that a rapid decrease in mean area is due to systems fracturing into multiple smaller systems.

The mean areas of the systems increase and decrease most rapidly at the start and end of their life cycles, following smooth parabolic curves. Analysis of when systems reach their maximum area (Figure S12) shows that this smooth curve is a result of averaging over systems that reach their maximum area at different points in their life cycles, with the modal time to reach the maximum area being approximately halfway through the system lifetimes. Interestingly, shorter-lived systems consistently show more rapid growth than longer-lived systems. They also consistently start and end with a larger mean area. Although larger systems grow less rapidly from a smaller initial area than smaller systems, they generally reach a larger maximum mean area because they grow for longer.

When the systems that start as children of existing systems or end by being accreted are included in the analysis (left column of Figure 6), the initial and final mean areas are consistently larger, but growth is slower, leading to a smaller maximum mean area. Similarly, inclusion of accreted and child systems leads to an increase in the fraction of systems that have maximum area at the start or end of their life cycle (Supplementary Figure S12). This becomes more pronounced for larger shorter-lived systems, which are more likely to be children or accreted (e.g., Figure 4). Systems may fracture and spawn child systems for various different physical reasons, and this may occur throughout the life cycle. However, fracturing is more common in the latter part of the life cycle when the system is decaying, which suggests that this fracturing may be due to the anvil cloud warming and/or dissipating, leading to brightness temperatures warmer than 233 K, which cause the previous single system to appear as multiple systems. Consequently, most child systems continue to decay and decrease in area, as seen for the shortest-lived large systems in Figure 6, which are almost all children. On the other hand, merging of systems is more likely in the earlier part of the life cycle when the systems are growing, as the anvils from multiple systems merge. Since most systems are growing when they are accreted, we see an increase in mean area at the end of the system lifetime. The shapes of the different curves in the left column of Figure 6 are determined by the proportion of the systems that are children, accreted, or neither.

Figure 7 follows a similar format to Figure 6, but instead of the life cycle of mean area it shows the life cycle of mean precipitation (per convective system pixel). Note that since precipitation estimates are often missing, the signal-to-noise ratio for the precipitation life cycle is much smaller than that for area. This is a particular problem for the longer-lived systems, which are least frequent, but account for more of the regional precipitation. Nevertheless, with the exception of the longest-lived small systems, mean precipitation appears to be most intense when the system is first detected and decreases consistently for the duration of the system. Combined with the life cycle of the system area, this pattern is consistent with the typical concept of a convective life cycle, with rapid intensification at the onset, followed by steady growth in size (as the storm matures and the anvil grows) and weakening in intensity until the dissipative stage. Finally, this figure shows that the increase in mean precipitation for larger systems identified in Section 4 is due to more intense mean precipitation throughout the life cycle.

From a satellite nowcasting perspective, the mean precipitation peaking at the point the systems are first identified is somewhat disappointing. It indicates that a more sophisticated approach is required to provide advance warning of the the most intense precipitation. However, the total precipitation per convective system timestep is the product of the mean precipitation and the system area.

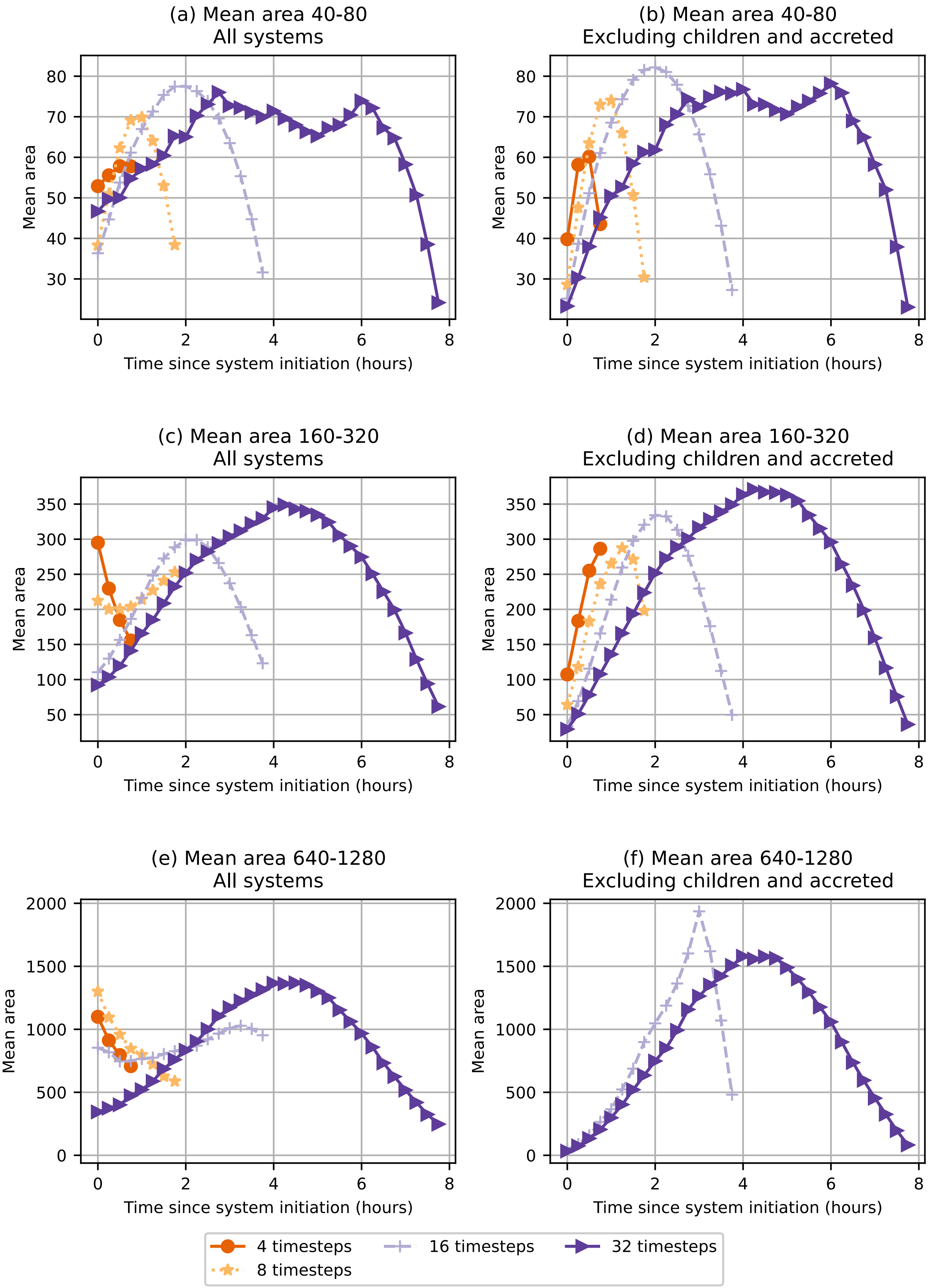

(a) Mean area 40-80
All systems

(b) Mean area 40-80
Excluding children and accreted

(c) Mean area 160-320
All systems

(d) Mean area 160-320
Excluding children and accreted

(e) Mean area 640-1280
All systems

(f) Mean area 640-1280
Excluding children and accreted

FIGURE 6 Composite mean area for each point in the life cycle. The three rows correspond to convective systems in three different mean area bins. The column on the left includes all convective systems, while the column on the right excludes those convective systems that are children (i.e., initiated by an existing system fracturing into multiple systems) or accreted (i.e., end by merging with an existing system). [Colour figure can be viewed at wileyonlinelibrary.com]

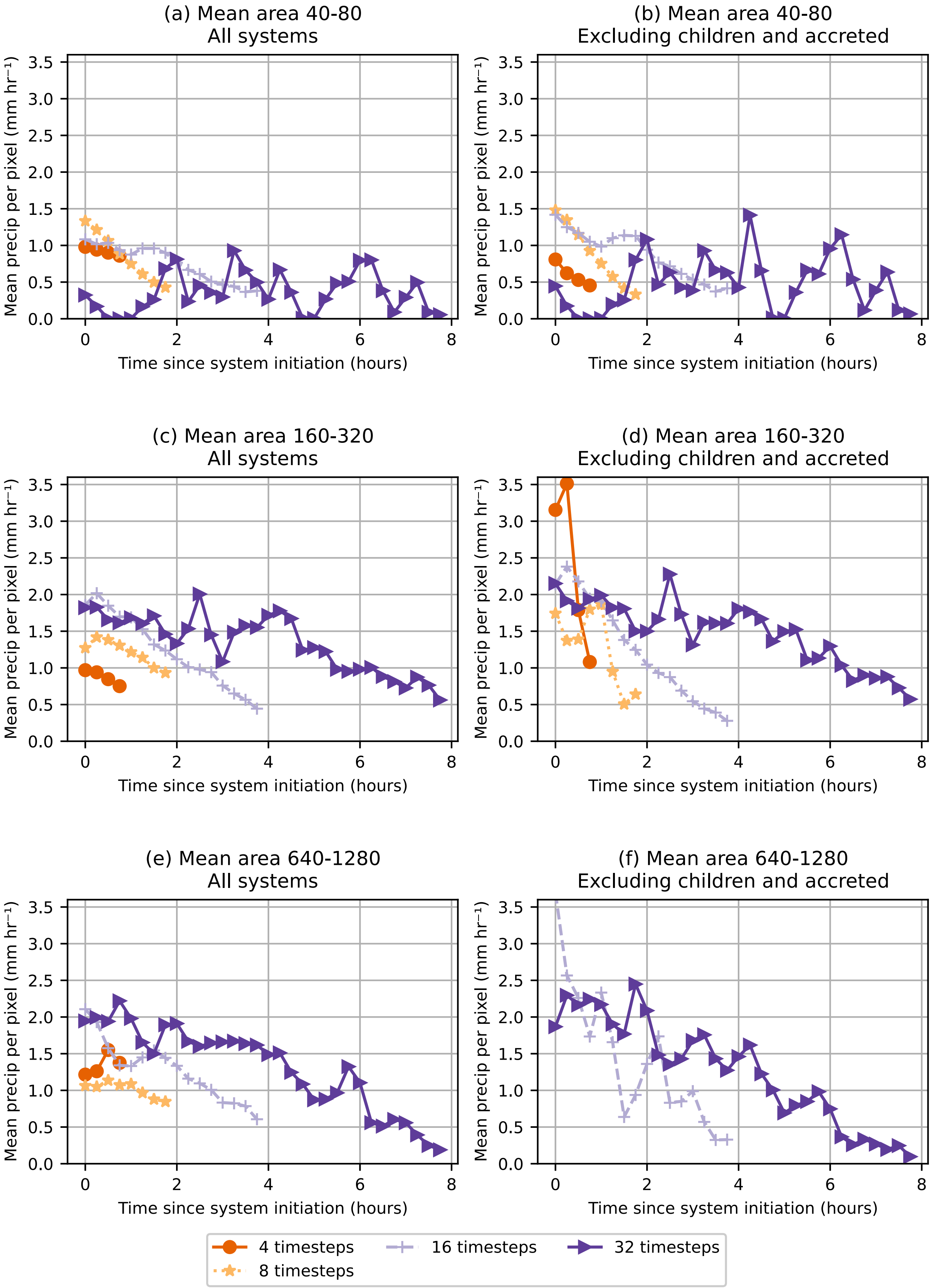

FIGURE 7 As Figure 6, but for composite mean precipitation for each point in the life cycle. [Colour figure can be viewed at wileyonlinelibrary.com]

Those systems that are not children of previous systems have largest mean area midway though their life cycle. Consequently, the total precipitation attributable to these systems peaks around one third of the way through the life cycle, indicating that there is some useful predictability that could be captured by a satellite nowcasting system.

6 | LINKS BETWEEN MJO PHASE, CONVECTIVE SYSTEM PROPERTIES, AND PRECIPITATION

As discussed in the Introduction, numerous studies have identified links between the MJO and East African rainfall (e.g. Pohl and Camberlin, 2006; Berhane and Zaitchik, 2014; Hogan *et al.*, 2014). In this section we investigate whether and how these known links between MJO and East African rainfall are manifested in the properties of convective systems. Such knowledge could feed into forecasting and nowcasting practices. This analysis focuses on the region from 10°S–10°N and 30°E–38°E, for which there is a known strong relationship between the MJO and rainfall, as described in Section 2.

Figure 8 shows the anomaly in daily mean rainfall, daily mean rainfall due to convective systems, and daily mean rainfall that is not attributed to convective systems as a function of MJO phase and four different seasons. Anomalies for each phase are calculated by subtracting the mean rainfall for all MJO phases and amplitudes from the mean rainfall for strong (MJO amplitude larger than one) MJO events in that phase. The impact of the MJO on precipitation in this region during the analysed period is consistent with previous studies (e.g. Hogan *et al.*, 2014). For both rainy seasons (MAM and OND) and the short dry season (JF), rainfall is anomalously high for MJO phases 1–3 and low for MJO phases 6–7. The MJO has less impact on the long dry season (JJAS) when the intertropical convergence zone and much of the precipitation is to the north of the region. A large fraction of the relationship between the domain mean precipitation and MJO phase is manifest in the precipitation that can be attributed to the tracked convective systems, while the nonconvective precipitation shows a much weaker dependence on MJO phase.

By changing perspective and considering the precipitation accumulated by each convective system over the course of its lifetime, we can understand how the MJO impacts on convective precipitation shown in Figure 8 are determined through changes in the properties of the convective systems. Note that in contrast to IMERG rainfall, which can be allocated to a specific day and consequently a single MJO phase, convective systems can persist from one day to another, with the potential for different MJO phases on each day. In the following analysis, the MJO phase corresponds to the time when each system is first identified. Moreover, whereas IMERG pixels are either within the analysis region or not, some convective systems may not be fully within the analysis region for their entire lifetime. The subsequent analysis includes all systems with centres falling in the region at any point in their life cycle. Consequently, the relationship between convective precipitation and MJO phase calculated using the convective system data (Figure 9) does not exactly match the relationship between convective precipitation and MJO phase calculated from an IMERG perspective (Figure 8). However, qualitatively the relationships are very similar.

For each season independently, using the tracked convective systems, the total precipitation R_{tot} associated with convective systems in phase p is given by

$$R_{\mathrm{tot}}(p) = \sum_{i=1}^{n(p)} R_{\mathrm{sys}}(i), \tag{2}$$

where there are $n(p)$ convective systems initiated in MJO phase p and $R_{\mathrm{sys}}(i)$ is the total precipitation associated with the convective system i. This can be rewritten as

$$R_{\mathrm{tot}}(p) = n(p) \times \overline{R_{\mathrm{sys}}(p)}, \tag{3}$$

that is, the total precipitation associated with convective systems in each phase $R_{\mathrm{tot}}(p)$ is the product of the number of systems in phase $n(p)$ and the mean integrated (i.e., over the system lifetime and area) precipitation per system $\overline{R_{\mathrm{sys}}(p)}$.

To facilitate a fair comparison of how the number of systems and mean integrated precipitation per system contribute to changes in the total precipitation with MJO phase, we normalise each by the mean of the other as follows:

$$n(p)_{\mathrm{norm}} = n(p) \times \frac{\sum_{p=1}^{8} \overline{R_{\mathrm{sys}}(p)}}{8}, \tag{4}$$

$$\overline{R_{\mathrm{sys}}(p)}_{\mathrm{norm}} = \overline{R_{\mathrm{sys}}(p)} \times \frac{\sum_{p=1}^{8} n(p)}{8}. \tag{5}$$

This normalisation results in consistent units and enables comparison of the normalised number of systems per phase and normalised mean integrated precipitation per system using the same axis. This is shown in Figure 9 along with the total convective system precipitation for each MJO phase. This reveals that the increase in total convective precipitation in phases 1–3 relative to 6–7 is due to increases in both the number of convective systems in these phases and the precipitation per system; both the number of systems and mean integrated precipitation per system follow a similar pattern to the total convective

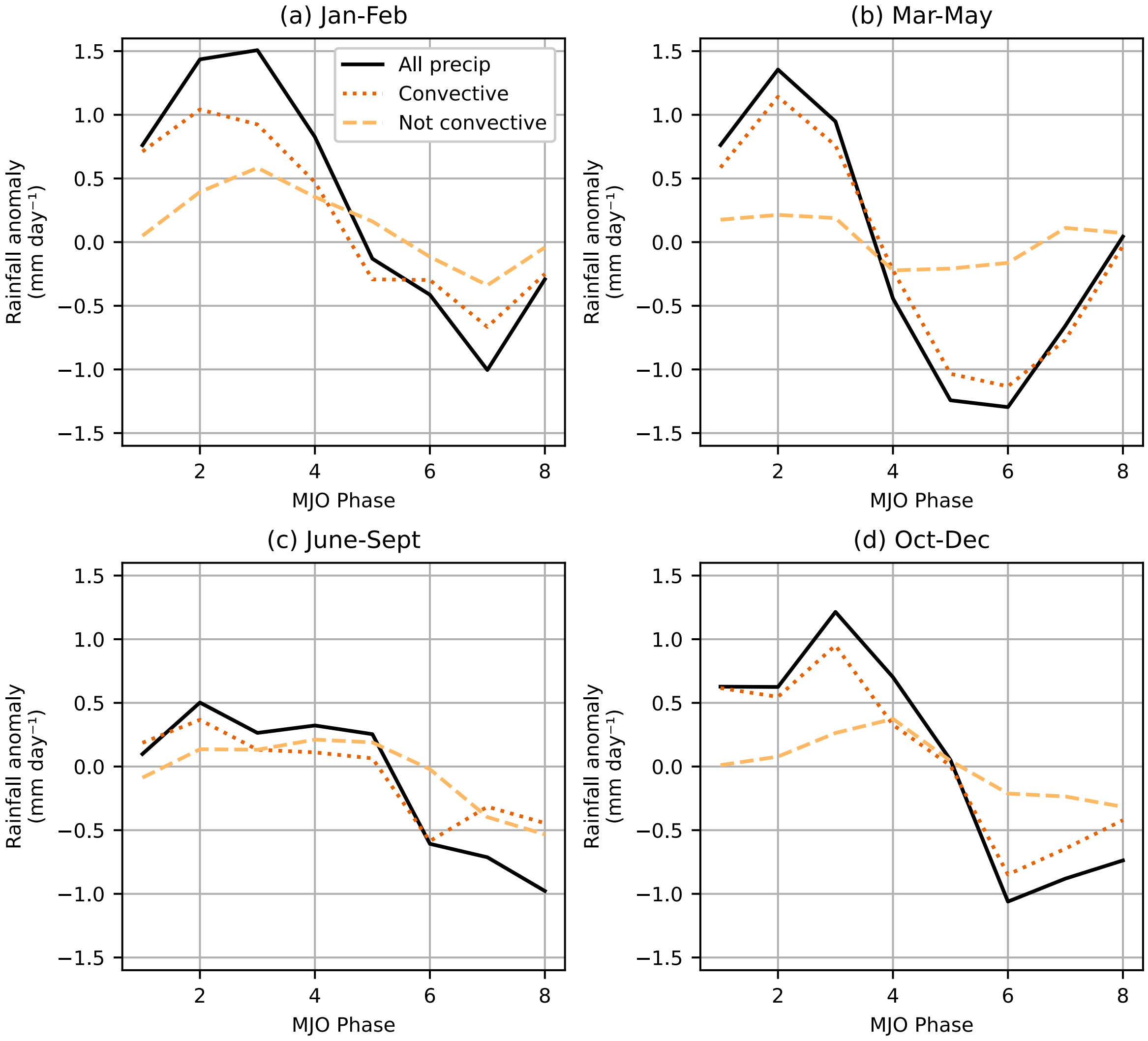

FIGURE 8 Rainfall anomaly for all IMERG pixels, pixels that correspond to a tracked convective system, and pixels that do not correspond to a tracked convective system, for the subset of the East Africa region bounded by 10°S–10°N and 30°E–38°E. [Colour figure can be viewed at wileyonlinelibrary.com]

precipitation, with larger values in phases 1–3 and smaller in phases 6–7. The normalised changes with MJO phase for each are of a similar magnitude, which is smaller than the amplitude of the change in total convective precipitation. The amplitude and direction of the changes in number of systems and mean integrated precipitation per system vary across the four seasons, but the sample size is too small to determine whether this is systematic or just random noise.

Similarly to Equation 3, the mean integrated precipitation can be decomposed as

$$\overline{R_{\mathrm{sys}}(p)} = \frac{\sum_{i=1}^{n(p)} \sum_{t=1}^{L(i)} \sum_{a=1}^{A(i,t)} R_{\mathrm{pix}}(i,t,a)}{n(p)}, \tag{6}$$

where $L(i)$ corresponds to the lifetime of convective system i, $A(i,t)$ denotes the area of convective system i at time t, and $R_{\mathrm{pix}}(i,t,a)$ is the rain rate for pixel a within the convective system i at time t. Defining the mean lifetime for convective systems in MJO phase p as

$$\overline{L(p)} = \frac{\sum_{i=1}^{n(p)} L(i)}{n(p)}, \tag{7}$$

the mean area of convective systems in MJO phase p as

$$\overline{A(p)} = \frac{\sum_{i=1}^{n(p)} L(i)\overline{A(i,:)}}{\sum_{i=1}^{n(p)} L(i)}, \tag{8}$$

and the mean intensity of convective systems in MJO phase p as

$$\overline{R_{\mathrm{pix}}(p)} = \frac{\sum_{i=1}^{n(p)} \sum_{t=1}^{L(i)} A(i,t)\overline{R_{\mathrm{pix}}(i,t,:)}}{\sum_{i=1}^{n(p)} \sum_{t=1}^{L(i)} A(i,t)}, \tag{9}$$

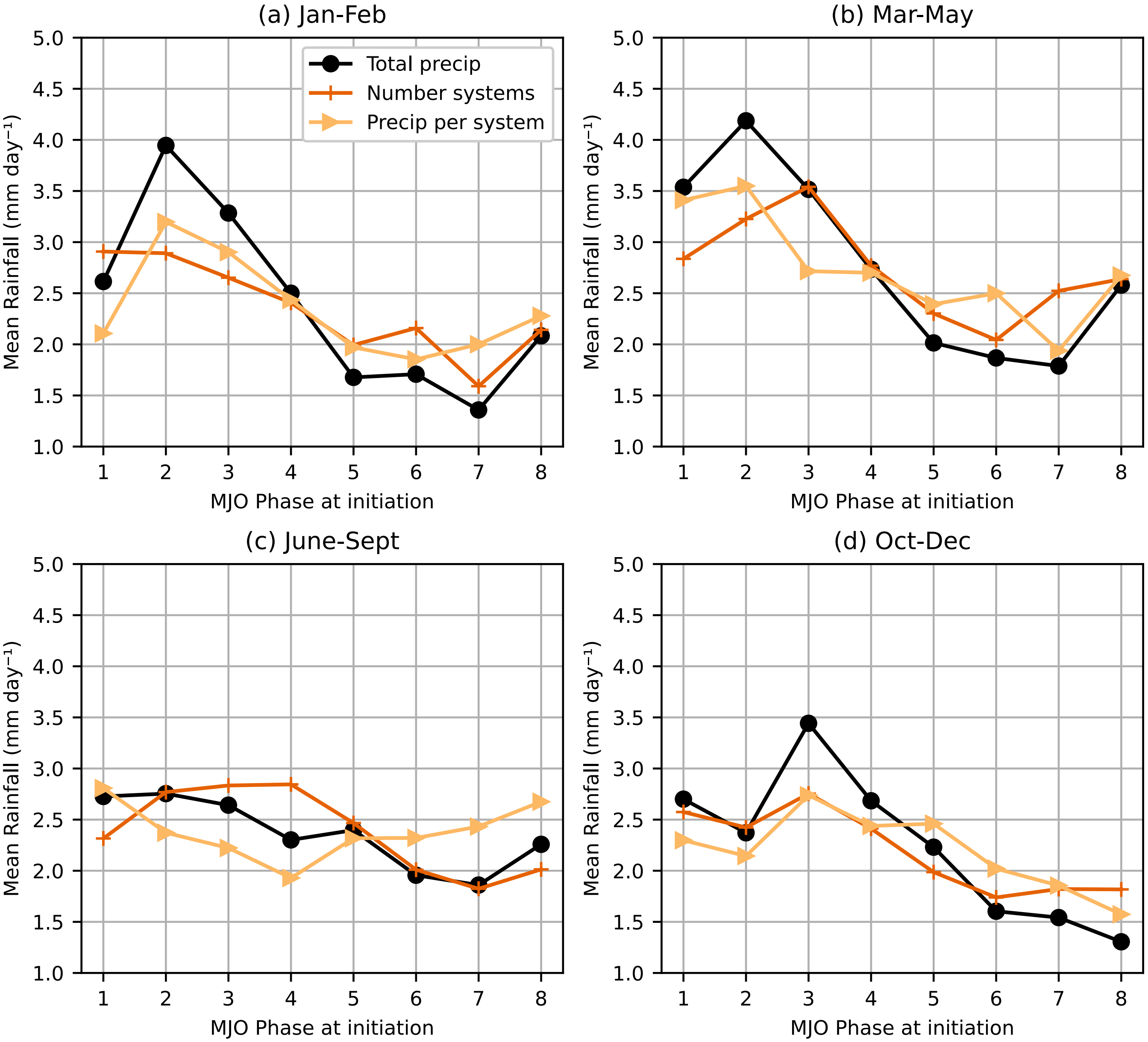

FIGURE 9 Contributions of different convective system properties to changes in total accumulated convective system daily mean rainfall in each MJO phase (black solid circles). To enable a fair comparison with consistent units, the mean accumulated rainfall per system and the number of systems are each normalised by the mean of the other, as described in the main text. For the subset of the East Africa region bounded by 10°S–10°N and 30°E–38°E. [Colour figure can be viewed at wileyonlinelibrary.com]

Equation 6 can be written as

$$\overline{R_{\mathrm{sys}}(p)} = \overline{L(p)} \times \overline{A(p)} \times \overline{R_{\mathrm{pix}}(p)}, \tag{10}$$

that is, the mean integrated precipitation per system is equal to the product of the mean system lifetime, the mean area of the systems and the mean intensity of precipitation per area and timestep. Note that since the lifetime and area vary from system to system, the mean area of the systems and mean intensity of precipitation per area and timestep are weighted by the lifetime of the system and the lifetime and area of the system, respectively, to ensure the equality holds.

Again, to ensure consistent units and ease comparison between the contributions of each of these quantities to the relationship between the mean integrated precipitation per system and MJO phase, we normalise each by the mean of the others as follows:

$$\overline{L(p)}_{\mathrm{norm}} = \overline{L(p)}\frac{\sum_{p=1}^{8}\overline{A(p)}}{8}\frac{\sum_{p=1}^{8}\overline{R_{\mathrm{pix}}(p)}}{8}, \tag{11}$$

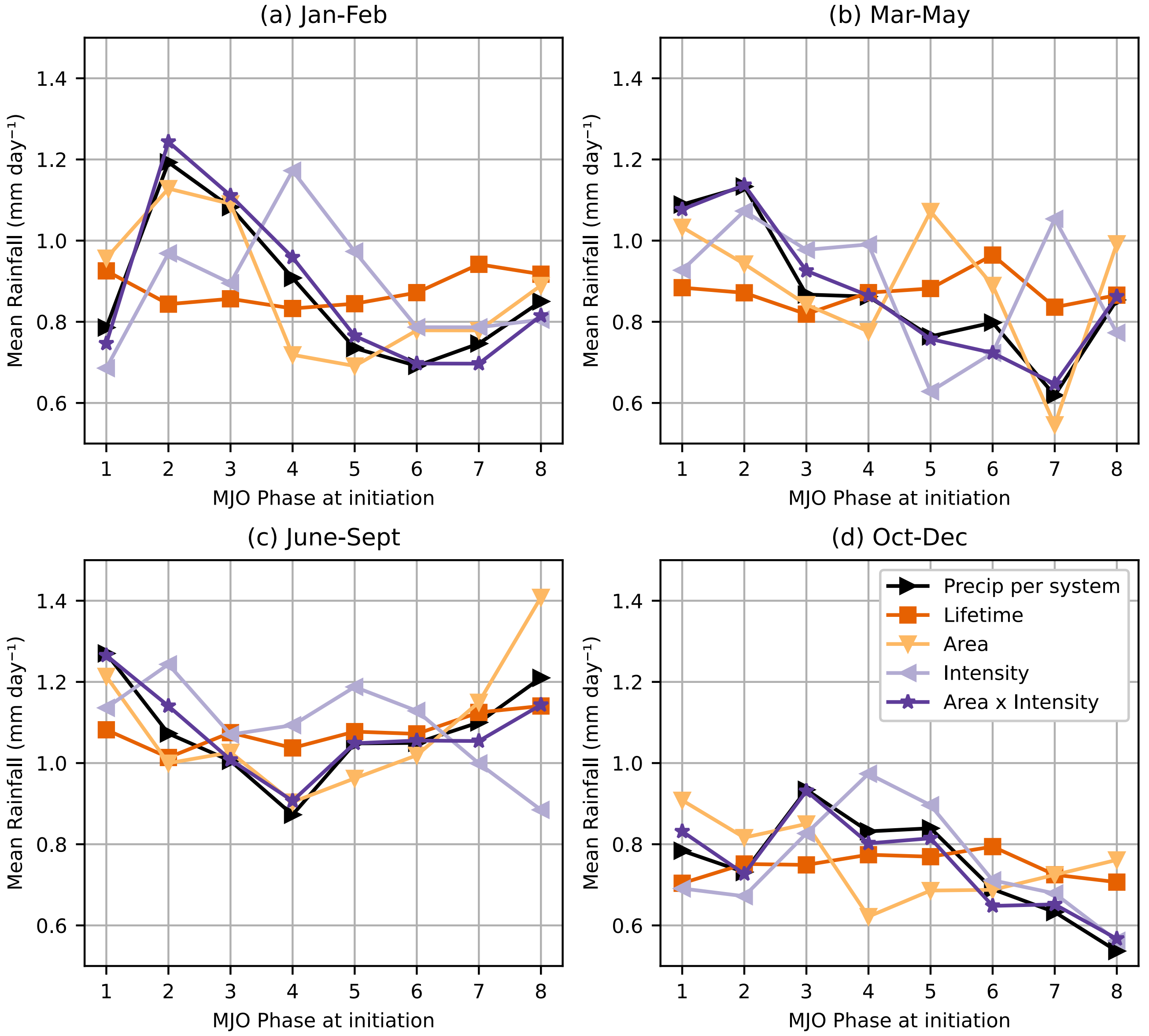

FIGURE 10 Contribution of different system properties to changes in mean accumulated precipitation per convective system in each MJO phase. To enable a fair comparison with consistent units, the different system properties are normalised by the means of the other properties as described in the main text. For the subset of the East Africa region bounded by 10°S–10°N and 30°E–38°E. [Colour figure can be viewed at wileyonlinelibrary.com]

$$\overline{A(p)}_{\mathrm{norm}} = \overline{A(p)}\frac{\sum_{p=1}^{8}\overline{L(p)}}{8}\frac{\sum_{p=1}^{8}\overline{R_{\mathrm{pix}}(p)}}{8}, \quad (12)$$

$$\overline{R_{\mathrm{pix}}(p)}_{\mathrm{norm}} = \overline{R_{\mathrm{pix}}(p)}\frac{\sum_{p=1}^{8}\overline{L(p)}}{8}\frac{\sum_{p=1}^{8}\overline{A(p)}}{8}. \quad (13)$$

These normalised quantities are shown in Figure 10. The relationship between the mean area and intensity of the systems and the MJO is rather noisy, with both showing maxima and minima at different MJO phases in the different seasons. Changes in mean area appear to be responsible for much of the changes in mean integrated precipitation per system with MJO phase in the two dry seasons, with Pearson product–moment correlation coefficients of 0.81 and 0.83 in JF and JJAS, respectively. On the other hand, it is difficult to see much of a relationship between the mean area and precipitation per system in the wet seasons, and indeed the correlation coefficients are much smaller, 0.56 and 0.13 in MAM and OND, respectively. The mean intensity follows a similar pattern to the mean integrated precipitation per system in OND (which is borne out by a correlation coefficient of 0.79), but there are no obvious relationships in the other seasons (correlation coefficients all less than 0.29 and negative in JJAS). The mean lifetime of convection shows much less variability between MJO phases than the other quantities, indicating that it does not play a large role in the variation in mean integrated precipitation per system with MJO phase. Moreover, correlations between the mean system lifetime and mean integrated precipitation per system are smaller than those of the other convective system properties. However, the product of the mean area and intensity of the systems (i.e., the mean integrated precipitation per system per timestep) explains almost all of the relationship between the precipitation per system and the MJO, with correlation coefficients larger than 0.94 in all seasons.

To summarise this section, the impact of the MJO on precipitation in the region from 10°S–10°N and 30°E–38°E during the analysis period is similar to that identified in previous studies. This relationship can largely be explained by changes in the convective precipitation with MJO phase, which in turn is due to changes in the number of convective systems and the product of the precipitation intensity and area of the systems. That is, the MJO provides a source of predictability for both the frequency and mean rainfall produced by convective systems in the region.

7 | SUMMARY

By combining a dataset of tracked convective systems based on infrared geostationary satellite data and rainfall estimates based on microwave measurements from polar-orbiting satellites, this article has investigated the links between convective systems, surface precipitation, and the MJO.

This study has demonstrated that most of the accumulated precipitation in East Africa is due to convective systems that are identified using a 233-K brightness-temperature threshold. However, this captures fewer than half the precipitation events; most of the light rainfall events, which are most frequent, do not correspond to an area of low brightness temperature. The fraction of rainfall events that coincide with convective systems increases with the intensity of the event. However, there is a great deal of spatial and temporal variability in the relationship between precipitation and convective systems in East Africa, due to interactions between surface features and convection.

Analysis of the relationships between precipitation and convective system properties has focused on the morphology of convective systems, in particular their size and duration. Larger systems tend to be longer-lived, with cases of large short-lived systems generally due to interactions between convective systems. Larger longer-lived systems have larger mean precipitation and are responsible for the majority of the regional precipitation. Compositing systems with the same lifetime and similar areas reveals that on average they increase in area initially, reaching a maximum half way through their lifetime, before the area decreases at a similar rate. Again, interactions between systems may lead to different behaviour. On the other hand, mean precipitation is most intense when a system is first detected and decreases throughout the lifetime of the system.

The well-established links between East African precipitation are due primarily to changes in convective system precipitation, with increased precipitation over the inland part of the region in early MJO phases due to more convective systems, each of which produces more rainfall on average. The increase in average rainfall per system is due to changes in the mean area of systems and the mean rainfall per convective system pixel. However, individually, both the mean system area and rainfall per system have rather inconsistent relationships with the MJO phase.

This study has focused primarily on the relationships between the size, lifetime, and precipitation attributed to convective systems. Further work could exploit the database of tracked convective systems further to understand convection in this region better. In particular, there are opportunities to look in more detail at other properties of the systems, such as changes in brightness temperature, to investigate predictability of future precipitation based on the initial properties of convective systems and to focus on intense precipitation, which has the most severe impacts.

AUTHOR CONTRIBUTIONS

Peter G. Hill: conceptualization; data curation; formal analysis; investigation; methodology; project administration; software; visualization; writing – original draft; writing – review and editing. **Thorwald H. M. Stein:** conceptualization; funding acquisition; methodology; software; supervision; writing – review and editing. **Carlo Cafaro:** methodology; writing – review and editing.

ACKNOWLEDGEMENTS

This work was supported by UK Research and Innovation as part of the Global Challenges Research Fund, African SWIFT programme, grant number NE/P021077/1. We thank two anonymous reviewers, who helped to improve this article.

ORCID

Peter G. Hill https://orcid.org/0000-0002-9745-2120
Thorwald H. M. Stein https://orcid.org/0000-0002-9215-5397
Carlo Cafaro https://orcid.org/0000-0001-8063-4887

REFERENCES

Arkin, P.A. (1979) The relationship between fractional coverage of high cloud and rainfall accumulations during GATE over the B-scale Array. *Monthly Weather Review*, 107, 1382–1387.

Ayugi, B., Zhihong, J., Zhu, H., Ngoma, H., Babaousmail, H., Rizwan, K. and Dike, V. (2021) Comparison of CMIP6 and CMIP5 models in simulating mean and extreme precipitation over East Africa. *International Journal of Climatology*, 41, 6474–6496.

Baidu, M., Schwendike, J., Marsham, J.H. and Bain, C. (2022) Effects of vertical wind shear on intensities of mesoscale convective systems over west and Central Africa. *Atmospheric Science Letters*, 23, e1094.

Berhane, F. and Zaitchik, B. (2014) Modulation of daily precipitation over East Africa by the Madden-Julian oscillation. *Journal of Climate*, 27, 6016–6034.

Bornemann, F.J., Rowell, D.P., Evans, B., Lapworth, D.J., Lwiza, K., Macdonald, D.M., Marsham, J.H., Tesfaye, K., Ascott, M.J. and Way, C. (2019) Future changes and uncertainty in decision-relevant measures of East African climate. *Climate Change*, 156, 365–384.

Cafaro, C., Woodhams, B.J., Stein, T.H.M., Birch, C.E., Webster, S., Bain, C.L., Hartley, A., Clarke, S., Ferrett, S. and Hill, P. (2021) Do convection-permitting ensembles Lead to more Skillful short-range probabilistic rainfall forecasts over tropical East Africa? *Weather and Forecasting*, 36, 697–716.

Camberlin, P. (2018) *Climate of Eastern Africa*. Oxford, UK: Oxford Research Encyclopedia of Climate Science.

Camberlin, P., Gitau, W., Planchon, O., Dubreuil, V., Funatsu, B.M. and Philippon, N. (2017) Major role of water bodies on diurnal precipitation regimes in eastern Africa. *International Journal of Climatology*, 38, 613–629.

Crook, J., Klein, C., Folwell, S., Taylor, C.M., Parker, D.J., Stratton, R. and Stein, T. (2019) Assessment of the representation of west African storm lifecycles in convection-permitting simulations. *Earth and Space Sciences*, 6, 818–835.

Dezfuli, A.K., Ichoku, C.M., Mohr, K.I. and Huffman, G.J. (2017) Precipitation characteristics in west and East Africa from satellite and in situ observations. *Journal of Hydrometeorology*, 18, 1799–1805.

Dixon, M. and Wiener, G. (1993) TITAN: thunderstorm identification, tracking, analysis, and nowcasting—a radar-based methodology. *Journal of Atmospheric and Oceanic Technology*, 10, 785–797.

Field, P.R. and Heymsfield, A.J. (2015) Importance of snow to global precipitation. *Geophysical Research Letters*, 42, 9512–9520.

Finney, D.L., Marsham, J.H., Jackson, L.S., Kendon, E.J., Rowell, D.P., Boorman, P.M., Keane, R.J., Stratton, R.A. and Senior, C.A. (2019) Implications of improved representation of convection for the East Africa water budget using a convection-permitting model. *Journal of Climate*, 32, 2109–2129.

Goyens, C., Lauwaet, D., Schröder, M., Demuzere, M. and Lipzig, N.P.M.V. (2011) Tracking mesoscale convective systems in the Sahel: relation between cloud parameters and precipitation. *International Journal of Climatology*, 32, 1921–1934.

Haile, G.G., Tang, Q., Sun, S., Huang, Z., Zhang, X. and Liu, X. (2019) Droughts in East Africa: causes, impacts and resilience. *Earth-Science Reviews*, 193, 146–161.

Han, L., Fu, S., Zhao, L., Zheng, Y., Wang, H. and Lin, Y. (2009) 3D convective storm identification, tracking, and forecasting—an enhanced TITAN algorithm. *Journal of Atmospheric and Oceanic Technology*, 26, 719–732.

Hanley, K.E., Pirret, J.S.R., Bain, C.L., Hartley, A.J., Lean, H.W., Webster, S. and Woodhams, B.J. (2021) Assessment of convection-permitting versions of the unified model over the Lake Victoria basin region. *Quarterly Journal of the Royal Meteorological Society*, 147, 1642–1660.

Hill, P.G., Stein, T.H., Roberts, A.J., Fletcher, J.K., Marsham, J.H. and Groves, J. (2020) How skilful are Nowcasting satellite applications facility products for tropical Africa? *Meteorological Applications*, 27, e1966.

Hodges, K.I. and Thorncroft, C.D. (1997) Distribution and statistics of African mesoscale convective weather systems based on the ISCCP Meteosat imagery. *Monthly Weather Review*, 125, 2821–2837.

Hogan, E., Shelly, A. and Xavier, P. (2014) The observed and modelled influence of the Madden-Julian oscillation on east African rainfall. *Meteorological Applications*, 22, 459–469.

Hou, A.Y., Kakar, R.K., Neeck, S., Azarbarzin, A.A., Kummerow, C.D., Kojima, M., Oki, R., Nakamura, K. and Iguchi, T. (2014) The global precipitation measurement mission. *Bulletin of the American Meteorological Society*, 95, 701–722.

Huffman, G.J., Bolvin, D.T., Braithwaite, D., Hsu, K., Joyce, R., Kidd, C., Nelkin, E.J., Sorooshian, S., Tan, J. and Xie, P. (2019) Nasa global precipitation measurement (gpm) integrated multi-satellite retrievals for gpm (imerg). In: *Algorithm Theoretical Basis Document, Version 06*. Washington, DC: NASA.

Johnson, D.B., Flament, P. and Bernstein, R.L. (1994) High-resolution satellite imagery for mesoscale meteorological studies. *Bulletin of the American Meteorological Society*, 75, 5–33.

Keat, W.J., Stein, T.H.M., Phaduli, E., Landman, S., Becker, E., Bopape, M.-J.M., Hanley, K.E., Lean, H.W. and Webster, S. (2019) Convective initiation and storm life cycles in convection-permitting simulations of the met office unified model over South Africa. *Quarterly Journal of the Royal Meteorological Society*, 145, 1323–1336.

Klein, C., Belušić, D. and Taylor, C.M. (2018) Wavelet scale analysis of mesoscale convective systems for detecting deep convection from infrared imagery. *Journal of Geophysical Research: Atmospheres*, 123, 3035–3050.

Kobusingye, O., Tumwesigye, N.M., Magoola, J., Atuyambe, L. and Alonge, O. (2016) Drowning among the lakeside fishing communities in Uganda: results of a community survey. *International Journal of Injury Control and Safety Promotion*, 24, 363–370.

Laing, A.G., Carbone, R., Levizzani, V. and Tuttle, J. (2008) The propagation and diurnal cycles of deep convection in northern tropical Africa. *Quarterly Journal of the Royal Meteorological Society*, 134, 93–109.

Laing, A.G. and Fritsch, J.M. (1993) Mesoscale convective complexes in Africa. *Monthly Weather Review*, 121, 2254–2263.

Laurent, H., D'Amato, N. and Lebel, T. (1998) How important is the contribution of the mesoscale convective complexes to the Sahelian rainfall? *Physics and Chemistry of the Earth*, 23, 629–633.

Li, C.-J., Chai, Y.-Q., Yang, L.-S. and Li, H.-R. (2016) Spatio-temporal distribution of flood disasters and analysis of influencing factors in Africa. *Natural Hazards*, 82, 721–731.

Liu, C. and Zipser, E.J. (2008) Diurnal cycles of precipitation, clouds, and lightning in the tropics from 9 years of TRMM observations. *Geophysical Research Letters*, 35, L04819.

MacLeod, D.A., Dankers, R., Graham, R., Guigma, K., Jenkins, L., Todd, M.C., Kiptum, A., Kilavi, M., Njogu, A. and Mwangi, E. (2021) Drivers and subseasonal predictability of heavy rainfall in equatorial East Africa and relationship with flood risk. *Journal of Hydrometeorology*, 22, 887–903.

Madden, R.A. and Julian, P.R. (1971) Detection of a 40–50 day oscillation in the zonal wind in the tropical Pacific. *Journal of the Atmospheric Sciences*, 28, 702–708.

Marcos, C., Sancho, J. and Tapiador, F. (2015) NWC SAF convective precipitation product from MSG: a new day-time method based on cloud top physical properties. *Thethys: Journal of Mediterranean Meteorology & Climatology*, 12, 3–11.

Milford, J. and Dugdale, G. (1990) Estimation of rainfall using geostationary satellite data. *Applications of Remote Sensing in Agriculture*, 97, 110.

Nicholson, S.E. (2017) Climate and climatic variability of rainfall over eastern Africa. *Reviews of Geophysics*, 55, 590–635.

Nicholson, S.E. (2018) The ITCZ and the seasonal cycle over equatorial Africa. *Bulletin of the American Meteorological Society*, 99, 337–348.

Omeny, P.A., Ogallo, L., Okoola, R., Hendon, H. and Wheeler, M. (2006) East African rainfall variability associated with the madden-Julian oscillation. *Journal of Kenya Meteorological Society*, 2, 105–114.

Pohl, B. and Camberlin, P. (2006) Influence of the Madden–Julian oscillation on east African rainfall. I: intraseasonal variability and regional dependency. *Quarterly Journal of the Royal Meteorological Society*, 132, 2521–2539.

Pohl, B., Camberlin, P. and Roucou, P. (2005) Typology of pentad circulation anomalies over the eastern Africa-Western Indian Ocean region, and their relationship with rainfall. *Climate Research*, 29, 111–127.

Roberts, A.J., Fletcher, J.K., Groves, J., Marsham, J.H., Parker, D.J., Blyth, A.M., Adefisan, E.A., Ajayi, V.O., Barrette, R., de Coning, E., Dione, C., Diop, A., Foamouhoue, A.K., Gijben, M., Hill, P.G., Lawal, K.A., Mutemi, J., Padi, M., Popoola, T.I., Rípodas, P., Stein, T.H. and Woodhams, B.J. (2021) Nowcasting for Africa: advances, potential and value. *Weather*, 77, 250–256.

Roberts, R.D., Goodman, S.J., Wilson, J.W., Watkiss, P., Powell, R., Petersen, R.A., Bain, C., Faragher, J., Chang'a, L.B., Kapkwomu, J.K., Oloo, P.N., Sebaziga, J.N., Hartley, A., Donovan, T., Mittermaier, M., Cronce, L. and Virts, K.S. (2022) Taking the HIGHWAY to save lives on Lake Victoria. *Bulletin of the American Meteorological Society*, 103, E485–E510.

Stein, T.H.M., Hogan, R.J., Hanley, K.E., Nicol, J.C., Lean, H.W., Plant, R.S., Clark, P.A. and Halliwell, C.E. (2014) The three-dimensional morphology of simulated and observed convective storms over southern England. *Monthly Weather Review*, 142, 3264–3283.

Tan, J., Petersen, W.A. and Tokay, A. (2016) A novel approach to identify sources of errors in IMERG for GPM ground validation. *Journal of Hydrometeorology*, 17, 2477–2491.

Taylor, C.M., Gounou, A., Guichard, F., Harris, P.P., Ellis, R.J., Couvreux, F. and Kauwe, M.D. (2011) Frequency of Sahelian storm initiation enhanced over mesoscale soil-moisture patterns. *Nature Geoscience*, 4, 430–433.

Wang, Y., Gueye, M., Greybush, S.J., Greatrex, H., Whalen, A.J., Ssentongo, P., Zhang, F., Jenkins, G.S. and Schiff, S.J. (2022) Verification of operational numerical weather prediction model forecasts of precipitation using satellite rainfall estimates over Africa. https://arxiv.org/abs/2201.02296.

Watkiss, P. and Cimato, F. (2021) Socio-Economic Benefits of the WISER Programme. https://www.metoffice.gov.uk/binaries/content/assets/metoffic%egovuk/pdf/business/international/wiser/wiser-seb-results_final-web.pdf.

Wheeler, M.C. and Hendon, H.H. (2004) An all-season real-time multivariate MJO index: development of an index for monitoring and prediction. *Monthly Weather Review*, 132, 1917–1932.

Whitworth, H.S., Pando, J., Hansen, C., Howard, N., Moshi, A., Rocky, O., Mahanga, H., Jabbar, M., Ayieko, P., Kapiga, S., Grosskurth, H. and Watson-Jones, D. (2019) Drowning among fishing communities on the Tanzanian shore of Lake Victoria: a mixed-methods study to examine incidence, risk factors and socioeconomic impact. *BMJ Open*, 9.

Wilson, J. and Roberts, R.D. (2022) Lake Victoria thunderstorms: radar-observed initiation and storm evolution modes. *Monthly Weather Review*, 150, 2485–2502.

Woodhams, B.J., Birch, C.E., Marsham, J.H., Lane, T.P., Bain, C.L. and Webster, S. (2019) Identifying key controls on storm formation over the Lake Victoria Basin. *Monthly Weather Review*, 147, 3365–3390.

Yang, W., Seager, R., Cane, M.A. and Lyon, B. (2015) The annual cycle of east African precipitation. *Journal of Climate*, 28, 2385–2404.

Young, M.P., Chiu, J.C., Williams, C.J.R., Stein, T.H.M., Stengel, M., Fielding, M.D. and Black, E. (2018) Spatio-temporal variability of warm rain events over southern West Africa from geostationary satellite observations for climate monitoring and model evaluation. *Quarterly Journal of the Royal Meteorological Society*, 144, 2311–2330.

SUPPORTING INFORMATION

Additional supporting information can be found online in the Supporting Information section at the end of this article.

How to cite this article: Hill, P.G., Stein, T.H.M. & Cafaro, C. (2023) Convective systems and rainfall in East Africa. *Quarterly Journal of the Royal Meteorological Society*, 149(756), 2943–2961. Available from: https://doi.org/10.1002/qj.4540